ARTICLES
PUBLISHED ONLINE: 4 JULY 2016 | DOI: 10.1038/NNANO.2016.95
nature nanotechnology

Optical imaging of individual biomolecules in densely packed clusters

Mingjie Dai[1,2], Ralf Jungmann[1,3†] and Peng Yin[1,3*]

Recent advances in fluorescence super-resolution microscopy have allowed subcellular features and synthetic nanostructures down to 10–20 nm in size to be imaged. However, the direct optical observation of individual molecular targets (~5 nm) in a densely packed biomolecular cluster remains a challenge. Here, we show that such discrete molecular imaging is possible using DNA-PAINT (points accumulation for imaging in nanoscale topography)—a super-resolution fluorescence microscopy technique that exploits programmable transient oligonucleotide hybridization—on synthetic DNA nanostructures. We examined the effects of a high photon count, high blinking statistics and an appropriate blinking duty cycle on imaging quality, and developed a software-based drift correction method that achieves <1 nm residual drift (root mean squared) over hours. This allowed us to image a densely packed triangular lattice pattern with ~5 nm point-to-point distance and to analyse the DNA origami structural offset with ångström-level precision (2 Å) from single-molecule studies. By combining the approach with multiplexed exchange-PAINT imaging, we further demonstrated an optical nanodisplay with 5 × 5 nm pixel size and three distinct colours with <1 nm cross-channel registration accuracy.

Biological and synthetic biomolecular systems exhibit complex structures at the nanoscale. Understanding the spatial arrangement of their individual components is critical for unravelling the molecular mechanism that underlies complex molecular behaviour (Fig. 1a). Super-resolution fluorescence techniques have bypassed the traditional diffraction limit and demonstrated imaging resolution down to 10–20 nm (refs 1–13). In particular, single-molecule localization microscopy (SMLM) builds up super-resolution images from single-emitter localizations and typically achieves photon-limited localization precision (down to ~1 nm) for single-emitter blinking events[13–15]. Previous single-molecule and SMLM studies separately demonstrated single-target visualization in isolation or in sparse arrangements[16,17], and high localization precision compatible with molecular-scale resolution[18–24]. However, the discrete visualization and precise localization of each individual molecular target (~5 nm) in a densely packed biomolecular cluster, which we refer to as 'discrete molecular imaging' (DMI), remains difficult.

Several factors limit the performance of current super-resolution techniques, such as the finite fluorophore photon budget, unsatisfactory fluorophore imaging efficiency, or limited control over target blinking kinetics[9,22,25–30]. These restrictions respectively translate to a limited photon count per localization, a limited number of blinking events per target and a high fraction of false localizations, which ultimately restrict the final imaging resolution, signal-to-noise ratio and the visualization of individual targets within dense clusters. Moreover nanometre-level accuracy stage noise and drift compensation is critical for high imaging resolution and quality.

We addressed the above challenge and demonstrated DMI using the DNA-PAINT super-resolution method[10,23,31–33] (Supplementary Fig. 1). DNA-PAINT, a variation of PAINT[9], exploits the transient binding of fluorophore-labelled imager strands to target-bound docking strands to achieve the necessary blinking for super-resolution reconstruction[10] (Fig. 1b; Supplementary Fig. 2). The continuous replenishment of imager strands renders DNA-PAINT immune to photobleaching, allowing high localization precision by extracting a large number of photons per single-molecule localization and a high target separability by collecting a large number of blinking events from each target. Additionally, due to independent and programmable control of blinking on- and off-rates, DNA-PAINT permits low imaging background in dense clusters from appropriately adjusted blinking duty cycle based on the target density (Fig. 1c).

We developed a framework for achieving DMI in the context of localization microscopy, including the technical requirements and quality assay methods (Supplementary Fig. 1). Specifically, we introduced an image-based assay for measuring the localization precision and the maximally achievable resolution, a target signal-to-noise ratio assay for measuring single-target separation and a method for estimating the fraction of false double-blinking localizations. We systematically studied their effects, and demonstrated stringent control for each of them with DNA-PAINT. In particular, we achieved a high localization precision (<1 nm single-molecule fitting precision, from up to 50,000 photons per single-molecule localization), a high target separability (from ~80 blinking events per target), a low imaging background using appropriately tuned blinking duty cycles and high-accuracy (<1 nm root mean squared (r.m.s.) over hours of imaging) microscope stage drift correction with a novel method based on synthetic nanostructure drift markers with designed geometric patterns. Finally, we used DMI to visualize individual targets in a compactly labelled molecular grid of targets (with a point-to-point spacing of ~5 nm) and demonstrated multiplexed DMI on a three-colour nanodisplay board with ~5 nm pixels.

Technical requirements for DMI

The technical requirements for DMI depend on the spatial distribution of the targets, particularly the closest spacing between targets and their local density[26,34] (within a diffraction-limited region, see Supplementary Note 7.1). Even with only two targets, a high localization precision that allows a full width at half maximum (FWHM) resolution equal to or smaller than the

[1]Wyss Institute for Biologically Inspired Engineering, Harvard University, Boston, Massachusetts 02115, USA. [2]Biophysics Program, Harvard University, Boston, Massachusetts 02115, USA. [3]Department of Systems Biology, Harvard Medical School, Boston, Massachusetts 02115, USA.
[†]Present address: Max Planck Institute of Biochemistry and LMU, Munich 82152, Germany. *e-mail: py@hms.harvard.edu

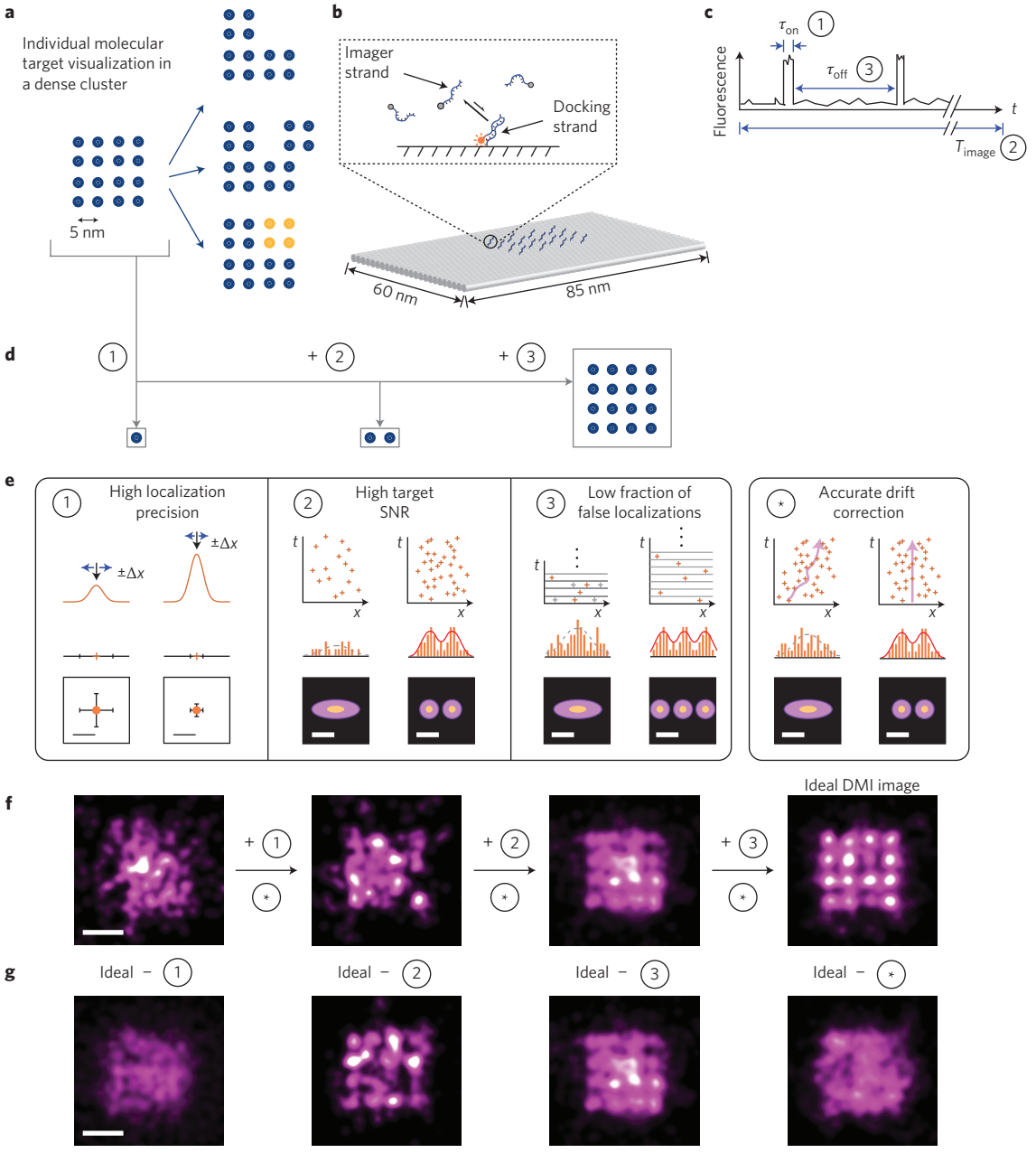

Figure 1 | Principle and requirements of DMI. a, The concept of super-resolution DMI, illustrated with a point array representation (blue dots represent individual molecular targets, yellow dots represent chemical modifications). Left: A regular 16-component biomolecular complex. Right: Its various structural and chemical variations. **b**, Illustration of the DNA-PAINT principle: transient binding between a docking strand and dye-conjugated imager strands (top) on a synthetic DNA nanostructure, where each cylinder represents a DNA double helix (bottom). **c**, Schematic DNA-PAINT blinking time trace of a single imaging target. The three blinking characteristics measure the blinking on-time τ_{on} (1), the total imaging time T_{image} (2) and the blinking off-time τ_{off} (3), and can be tuned to meet the three blinking requirements in **e**. **d**, Schematics of different substructures from the complex in **a**: a single target (left), a pair of targets in close proximity (middle) and a dense lattice (right). All need different blinking requirements in **e** to be clearly visualized. **e**, Technical requirements for achieving discrete molecular imaging. Each panel outlines one technical requirement and schematically depicts the effect on imaging quality before (left column) and after (right column) the requirement is satisfied. For requirement (1), the intensity profile in 1D (top), fitted Gaussian centres in 1D (middle) and 2D (bottom) are shown. For requirements (2), (3) and (*) the localization time trace in 1D (top), localization histogram in 1D (middle) and 2D (bottom) are shown. The orange lines and crosses indicate localizations. The orange bars depict localization histograms. The solid red lines and dotted grey lines indicate successful and failed Gaussian fittings on localization histograms, respectively. For (3), grey crosses indicate true localizations eclipsed by false double-blinking localizations. The same numbering for technical requirements (1)–(3) is also used in Fig. 2, Table 1 and Supplementary Fig. 3. **f**,**g**, Simulations of the imaging effects of the technical requirements for the complex in **a** under increasingly improved imaging conditions without stage drift (**f**) or under non-ideal imaging conditions with one of the four requirements unsatisfied (**g**). See Methods and Supplementary Methods 2 for simulation details, and Supplementary Note 7 for discussions. Scale bars, 5 nm (**e**); 10 nm (**f**,**g**).

spacing between them is necessary but not sufficient for their clear separation[23,35]. Targets arranged in dense clusters impose even more stringent requirements. Although general requirements and quality guidelines for super-resolution imaging have been discussed[26,27,34,36], a systematic formulation of the technical requirements for DMI and its quality control methods is still lacking.

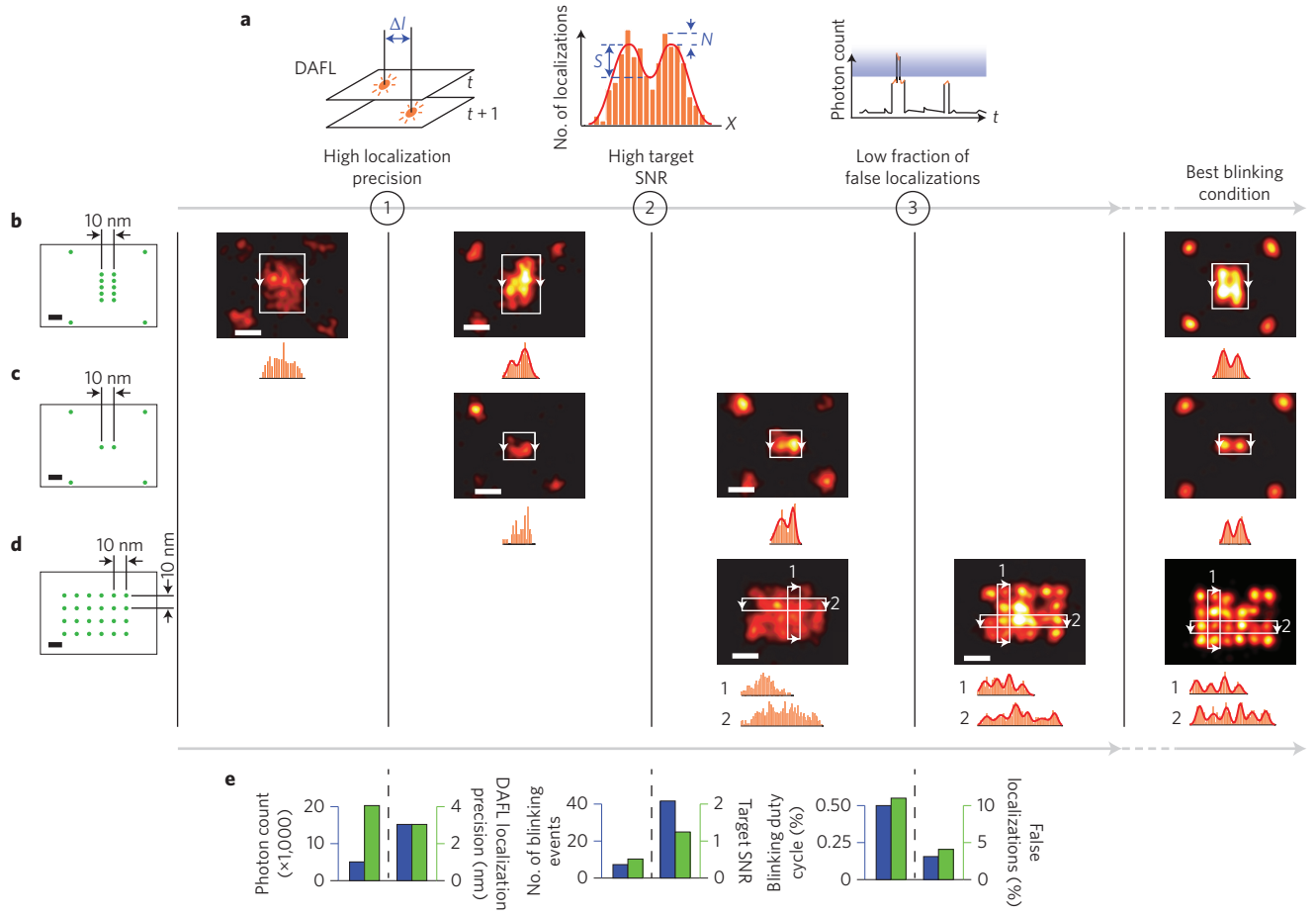

Figure 2 | Systematic characterization of the blinking requirements and optimization of the DNA-PAINT imaging quality. a, Methods for the systematic characterization of the three blinking requirements depicted in Fig. 1. (1) DAFL measures the distance (ΔI) between pairs of spatially close localizations originating from adjacent camera frames. (2) Target SNR measures the separability of the peaks in the localization histogram in the super-resolved image. *S*, signal; *N*, noise. The red curve indicates the two-peak Gaussian fit. (3) The photon count cut-off in the blinking trace measures the fraction of false localizations. The blue shaded area indicates identified false localizations. The orange markers, bars and curves indicate localizations, histograms and time traces, respectively. **b**–**d**, Designed DNA origami standards with 10 nm spacing under different blinking conditions. The left column shows the design schematics of the DNA origami standards; green dots indicate DNA-PAINT docking strands; four corners in **b**,**c** are used as alignment markers. The right columns show DNA-PAINT images under increasingly better blinking conditions (one condition per column). The histograms below the images show the projection profiles from the areas indicated by white boxes along the directions of arrows. **e**, Quantitative characterization and pairwise comparisons of the imaging conditions used in **b**–**d** before and after meeting each extra requirement, assayed with the methods in **a**. For each comparison, the left *y* axis (blue) shows the control parameter and right *y* axis (green) shows the experimental measurement. For more details see Supplementary Figs 4–6 on origami designs, Supplementary Figs 7–14 for super-resolution images, Methods and Supplementary Methods 3 and 5 for DNA-PAINT imaging conditions and analysis methods. Scale bars, 10 nm in schematics and 20 nm in super-resolution images.

We examined the technical requirements for DMI with an example square lattice pattern (Fig. 1d). It is increasingly more difficult to discretely identify and precisely position a single isolated target (Fig. 1d, left), a pair of targets in close proximity (middle) and finally a dense lattice of targets (right), thus requiring increasingly more stringent imaging conditions (Fig. 1e). These four conditions are described as follows. Requirement (1): A high localization precision. This can be obtained by collecting a high photon count per single-molecule localization, and allows the precise localization of an isolated target. Requirement (2): A high target signal-to-noise ratio (target SNR) in the super-resolved image. This can be achieved by collecting a large number of blinking events per molecular target, and allows for a clear separation between two nearby targets. Requirement (3): A low fraction of false localizations from double-blinking events. This can be achieved by using a low blinking on–off duty cycle, which minimizes falsely localized background noise and hence allows the discrete visualization of each target within a densely packed complex. Lastly, requirement (*): An accurate compensation mechanism for microscope stage drift. This is important for the accurate identification and localization of any molecular structures of interest, especially over extended imaging times. Computer-simulated super-resolution images reveal increasingly better image qualities when more of these requirements are satisfied (Fig. 1f) and that each of the four requirements is indispensable for DMI (Fig. 1g). See online methods, Supplementary Method 2 and Supplementary Note 7.2 for details.

We termed requirements (1)–(3) collectively the three blinking requirements, as they can all be met by appropriate single-molecule blinking properties (see Fig. 1c). As DNA-PAINT allows flexible tuning of target blinking kinetics, it therefore provides a promising route for implementing DMI.

Systematic characterization and quality control for DMI

To quantitatively characterize the effects of the above DMI requirements on imaging quality, we proposed a set of assay methods (Fig. 2a): (1) an image-based assay of the localization precision

and the maximal achievable resolution by comparing the positions of super-localized centres from neighbouring frames (termed the distance between adjacent-frame localizations, or DAFL); (2) a target SNR assay based on the analysis of the distribution of super-localized centres, which directly measures the separability of neighbouring targets in super-resolved images; and (3) a localization time trace-based assay for estimating the false localization ratio. These assay methods provide a general, sample-agnostic method for the stringent quality control of general super-resolution microscopy studies as well as DMI (see Methods, Supplementary Fig. 3 and Supplementary Methods 3 for details).

Using these assay methods, we first simulated super-resolution movies with varying photon counts, numbers of blinking events and blinking duty cycles, and measured the resultant single-molecule localization precision, the target SNR and the fraction of false localizations from double-blinking events (see Methods, Supplementary Fig. 3 and Supplementary Methods 2 and 3 for details). We observed a high localization precision (<1 nm, supporting <2 nm FWHM resolution) with a high photon count (>30,000), a consistent target separation with a high target SNR (>2 under our definition) and low background noise under a low fraction of false localizations (down to <5%), allowing DMI imaging.

Applying the same assay methods, the three blinking requirements (localization precision, target SNR and false localization ratio) for DMI were each experimentally verified by subjecting synthetic DNA origami nanostructure[37,38] standards with three designed target patterns to different DNA-PAINT imaging conditions (Fig. 2b–d: the leftmost columns are the designed pattern schematics; the five right columns are DNA-PAINT images, see Methods and Supplementary Methods 4 for details). Synthetic DNA nanostructures provide a programmable and geometrically precise molecular patterning platform for single-molecule and super-resolution studies. These structures were self-assembled from a long single-stranded DNA scaffold and a collection of short staple strands[37]. By extending a selected subset of these staple strands, DNA-PAINT docking strands could be arranged into user-prescribed, geometrically precise nanopatterns and used as super-resolution imaging standards or auxiliary markers (see the next section, Supplementary Figs 4–6 and Supplementary Note 8 for details).

In Fig. 2b, two 10-nm spaced lines (each consisting of 5 points, spaced 5 nm apart to satisfy the Nyquist criterion) only turned from unresolvable speckles (left image) to separable lines (right image) with an increased photon count per single-molecule localization and hence a higher localization precision. However, the high localization precision alone under this imaging condition failed to resolve two points spaced by 10 nm (Fig. 2c, left image) due to the reduced number of targets (from 5 to 1 on each side). The two points only became resolvable (Fig. 2c, right image) with a larger number of blinking events per target and hence an increased target SNR. However, this imaging condition (with a high localization precision and target SNR) still failed to resolve a 24-target 10-nm grid (Fig. 2d, left image) due to the increased target density. The grid points only became individually resolvable (Fig. 2d, right image) with a decreased blinking duty cycle and hence a lower false localization ratio. Quantitative pairwise comparisons of these imaging conditions and the imaging quality assay results before and after meeting each of the three blinking requirements are shown in Fig. 2e (see Methods, Supplementary Figs 7–12 and Supplementary Methods 5.1 and 6.1 for details). Finally, we imaged these structures under the best imaging conditions and obtained clear images of the designed patterns (Fig. 2b–d, rightmost column, see Supplementary Figs 13 and 14 for details).

Subnanometre accuracy software-based drift correction

DMI also imposes stringent requirements on microscope stage drift compensation. For example, the clear separation of targets with 5 nm target-to-target spacing requires an accurate drift correction of <1 nm (r.m.s. drift) due to the compounded effects of stage drift and finite localization precision (assuming 1 nm localization precision, Fig. 3a; see Methods and Supplementary Methods 2 for details). Previous solutions either used an active feedback system to reach <1 nm residual drift, which requires a complicated hardware set-up and is technically involved to implement[21], or used software-based post-processing methods with embedded nanoparticle fiducial markers, which are typically limited by imperfect tracking accuracy[5,7,22] and do not support DMI resolution (~5 nm).

We demonstrate a novel, synthetic nanostructure fiducial marker-based stage drift correction and noise compensation method—termed templated drift correction—which achieves high-accuracy drift and noise cancellation (<1 nm r.m.s. residual drift) over both short and long timescales (from subsecond to ~5 h), without using specialized hardware. The key principle is to use super-resolved single-molecule targets (such as a single DNA docking strand) on pre-designed geometrically precise nanopatterns (such as a DNA nanostructure) as drift markers (Fig. 3b). Unlike conventional fiducial markers, these single-target drift markers possess unique advantages as they can be stably anchored on the surface, localized with high precision and without bleaching, flexibly rotatable around their anchor points (thus avoiding the fixed-dipole effect) and free of offset from the fluorescence centre to the drift marker centre position, such as in micrometre-sized beads and previous DNA origami drift markers[10,31]. We arranged these single-target markers in pre-designed, well-separated nanopatterns (the templates) to help pack a number of single-target markers within a diffraction-limited area and to allow their identification and separation during software processing steps (Fig. 3b). Moreover, the precise geometry of a nanopattern correlates all of the single-target drift markers on this pattern and effectively increases their on-fraction (the fraction of time that the marker is bright), producing a more accurate drift correction. We term this method geometry-templated drift correction.

We designed a square lattice pattern with 20 nm spacing as our nanopattern template to implement this strategy (Fig. 3c): a grid consists of 12 targets (docking strands), each of which will be treated as a single-target drift marker. After performing DNA-PAINT imaging and applying a round of simple trace-averaging drift correction, all 12 targets are clearly separated from each other in the reconstructed image, allowing them to serve as single-target drift markers (Fig. 3d, see also Supplementary Fig. 15). Note that the missing grid points were probably due to defects in the origami self-assembly or DNA synthesis (see Supplementary Note 9.1 for discussion), rather than imaging incompleteness. Single-particle analysis confirmed the completeness of the nanopattern and showed a high degree of regularity of the grid geometry as designed (Fig. 3e, see Methods, Supplementary Fig. 16 and Supplementary Method 6.2 for details). Specifically, we performed two-dimensional (2D) Gaussian fitting on each grid point followed by a regular grid fit to these 12 Gaussian-fitted centres, and observed that the average deviation between the Gaussian-fitted and regular grid-fitted centres was well below 1 nm (<0.30 nm r.m.s., Fig. 3f; see Methods, Supplementary Methods 6.2 and Supplementary Note 9.2 for details).

We then tested the performance of templated drift correction on the grid structures using the analysis workflow in Fig. 3i (left arrow, see Methods and Supplementary Methods 5.2 for details). Briefly, we first identified a pool of separable single-target drift markers, extracted their blinking time traces and determined the expected centre position for each target. Then for every frame we collected all of the localizations originating from these drift markers and calculated a global, photon-weighted average of 'offset vectors' from each localization to its expected centre position and used it as the drift correction vector. Single-particle analysis after templated drift correction showed a sharper image of the grid (Fig. 3g).

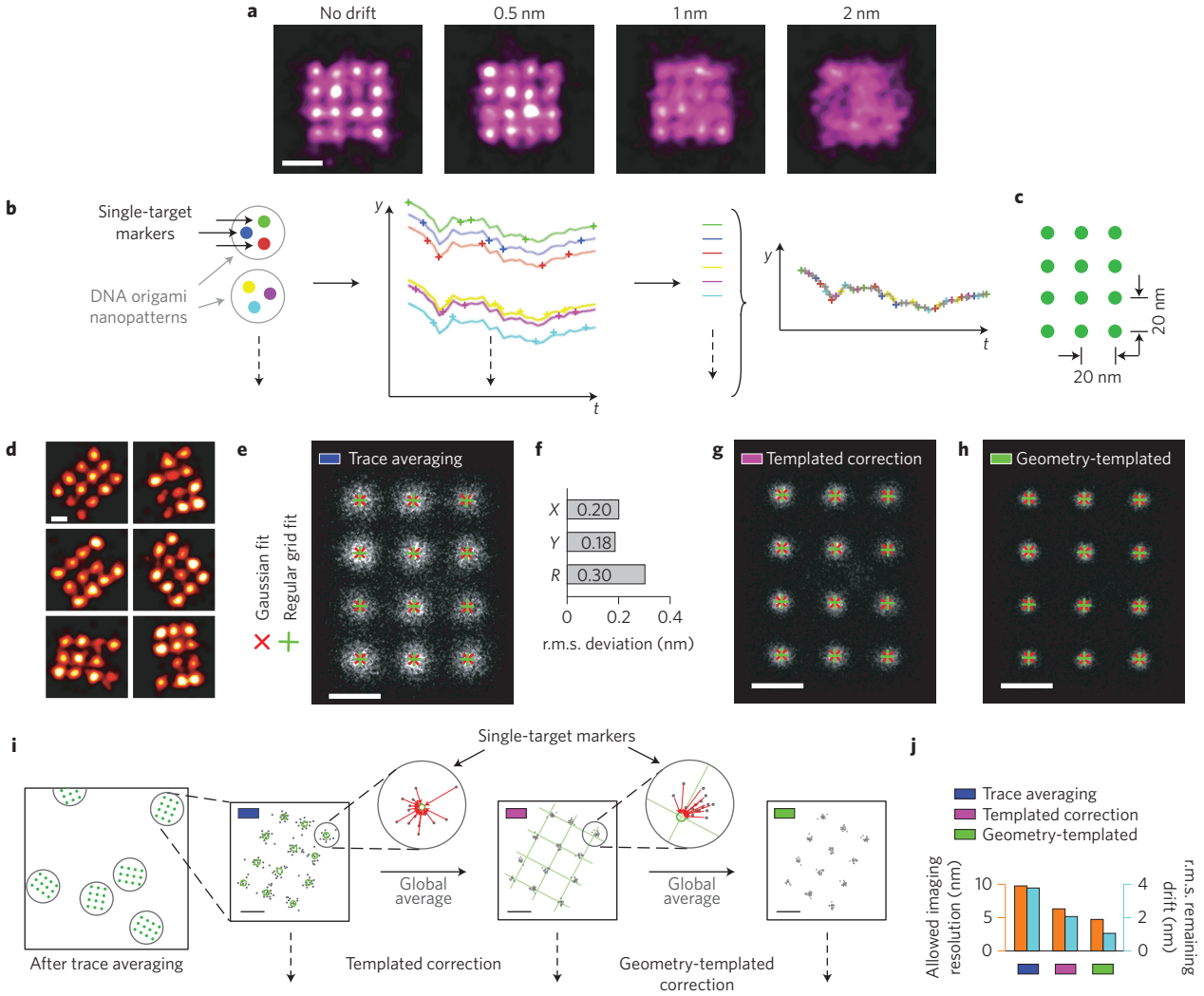

Figure 3 | Principle and performance of DNA nanostructure templated drift correction. a, The effect of drift on imaging quality is simulated for the biomolecular complex in Fig. 1a with 1 nm localization precision and different levels of stage drift. The structure can only be clearly visualized with 1 nm (r.m.s.) of drift or less. **b**, The principle of the templated drift correction method with pre-designed nanostructure patterns. Illustrating a three-target marker example, the schematics show a nanopattern design with single-target markers (left), the localization time traces from individual single-target markers (middle) and averaged drift correction trace after combining the traces from many markers (right). The targets and traces are colour-matched. Dashed arrows indicate many more structures used for drift correction. **c**, Design schematic of a 3 × 4 square grid with 20 nm point-to-point spacing on a DNA origami nanostructure. Each green dot indicates a docking strand. **d**, Representative DNA-PAINT super-resolution images of the 20 nm grid structure in **c** imaged with 300 ms frame time, 30,000 total frames and 3 nM imager strands. Missing grid points were probably due to synthesis or incorporation defects (see Supplementary Note 9.1 for more discussion). **e**, Single-particle averages of 20 nm grid images ($n = 700$) after trace averaging. The overlaid crosses indicate Gaussian fitted centres and regular grid-fitted centres using the red crosses as fitting targets. **f**, Root-mean-square (r.m.s.) deviation between the Gaussian fitted and regular grid-fitted centres in **e** in *X*, *Y* projections and 2D distance. **g**,**h**, Single-particle averages of the 20 nm grid images ($n = 700$) after templated (**g**) and geometry-templated (**h**) drift correction. The overlaid crosses indicate Gaussian fitted and regular grid-fitted centres as in **e**. The same colour code for different stages of drift correction in **e**,**g** and **h** are also used in **i**,**j** and Fig. 4. **i**, Procedure for templated and geometry-templated drift correction with 20 nm grid structures as templates. The schematics show a large field-of-view image with many drift markers after simple trace averaging (left). Each grey circle indicates a 20 nm drift marker. Three zoomed-in (squares) schematics show a super-resolved 20 nm grid marker after simple trace averaging (left), after templated drift correction (middle) and after geometry-templated correction (right). Dashed arrows indicate many more structures used for drift correction. Further zoomed-in schematics (circles) show one single-target marker and the calculation of the offset vectors. In the zoomed-in schematics (both squares and circles) grey dots indicate localizations, green dots and lines indicate Gaussian-fitted centres and regular grid-fitted lattices as guides for templated and geometry-templated drift correction calculations, and the red lines represent the calculated offset vectors. **j**, Comparison of the allowable imaging resolution (measured in FWHM, orange) and estimated remaining drift (turquoise) at different stages of drift correction. For more details, see Methods and Supplementary Methods 2 and 5 for the simulation and analysis methods, and Supplementary Fig. 15 for the super-resolution images. Scale bars, 10 nm (**a**); 20 nm (**d**,**e**,**g**,**h** and zoomed-in images in **i**).

Furthermore, the superior regularity of these 20 nm grid structures allowed us to perform another round of geometry-templated drift correction, again using these structures as drift markers (Fig. 3i, second arrow; see Methods and Supplementary Methods 5.2 for details), and producing an even sharper single-particle averaged image (Fig. 3h). We also compared the imaging resolution before and after templated and geometry-templated drift corrections, respectively, and estimated <1 nm (r.m.s.) residual drift after templated and geometry-templated corrections (Fig. 3j; see Methods and Supplementary Methods 6.2 for details).

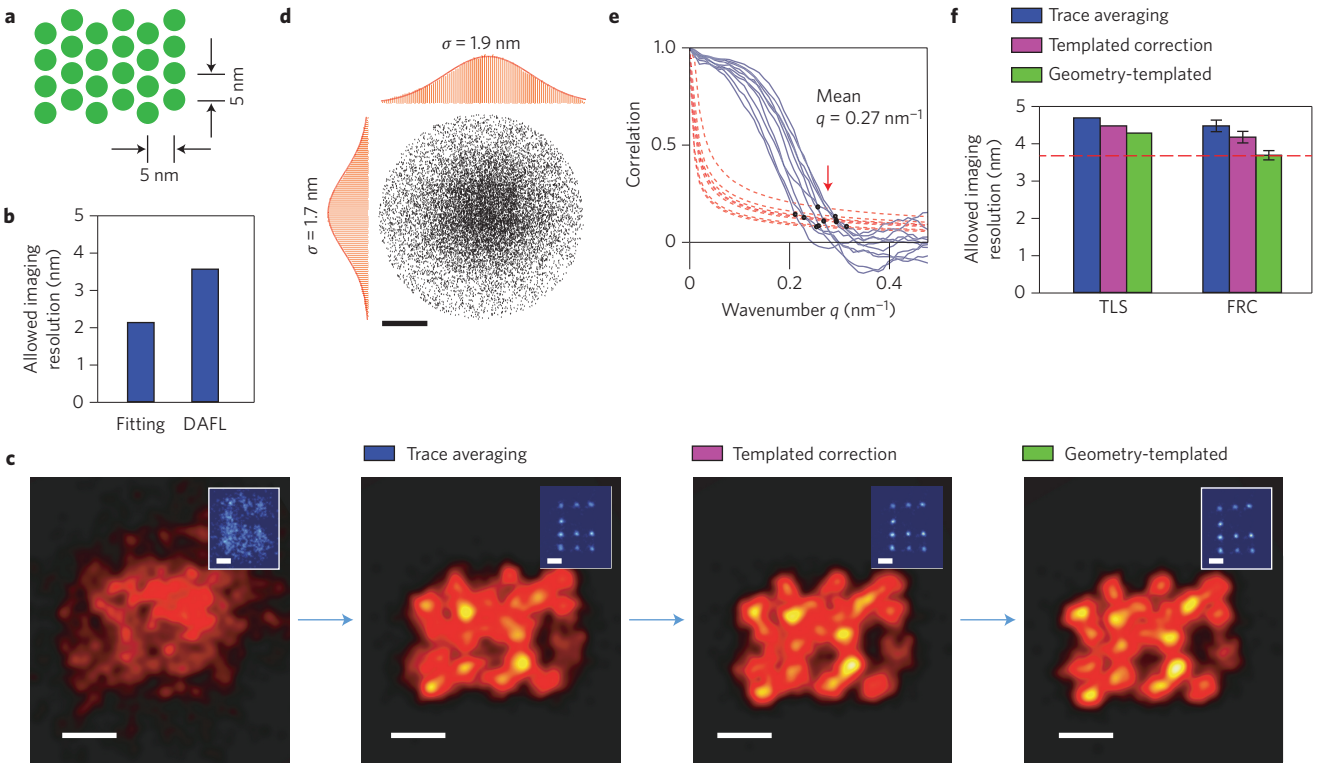

Figure 4 | Systematic quality analysis of 5 nm grid super-resolution image. a, Design schematics of a 4 × 6 triangular grid structure with ~5 nm point-to-point spacing on a DNA origami nanostructure. Each green dot indicates a docking strand. **b**, Allowable imaging resolution assayed by two methods before drift correction: single-molecule fitting uncertainty and DAFL, both measured in FWHM. **c**, Comparison of the DNA-PAINT images of a 5 nm grid structure and a 20 nm grid drift marker (blue, inset) at different stages of drift correction. **d**,**e**, Measured imaging resolution assayed by two methods after drift correction. **d**, Target localization spread (TLS), where the point cloud shows the overlapped localizations from individually separable targets aligned by the centre of mass. Histograms are shown for the horizontal (left) and vertical (top) projections. The red curves indicate Gaussian fits. **e**, Fourier ring correlation (FRC). The correlation curves (blue solid lines) and noise-based cutoff (red dotted lines) are shown for 10 representative images; black dots indicate crossing points. **f**, Comparison of the measured imaging resolution at different stages of drift correction assayed by TLS and FRC. The red dashed line indicates the localization precision-limited best allowable resolution (as determined by DAFL). The DNA-PAINT imaging conditions used for this experiment were 400 ms frame time, 40,000 total frames and 1 nM imager strand concentration. See Methods, Supplementary Figs 17–21 and Supplementary Methods 3 and 5 for more details on the assay methods and results. Scale bars, 10 nm in the images in **c**, 20 nm in the insets in **c**; and 2 nm in **d**.

Note that during templated and geometry-templated drift correction processes the global average of all of the offset vectors calculated from many origami grids across the entire field of view (rather than those from a single origami grid) was used for drift correction. In addition, although here we treat the 20 nm grid as both drift markers and imaging samples, in general applications (such as the 5 nm grid image in the next section) no previous knowledge of the imaging sample is required—only that of the origami grid markers is used.

5 nm grid DMI and analysis

To demonstrate the imaging capability of DMI, we designed a triangular grid structure with ~5 nm point-to-point spacing (Fig. 4a). This is the densest clustering pattern possible on our origami breadboard[37] and it also mimics the monomer spacing and arrangement in a microtubule segment (with a ~5 × 4 nm monomer size)[39].

Compared with the 10 nm grid images (Fig. 2b–d), the higher target density in this sample imposes more stringent imaging conditions—namely, an even higher photon count, a larger number of blinking events per target and a lower blinking duty cycle. We used a short (7 nt) docking strand to accommodate the high target density and to avoid potential spatial cross-talk between neighbouring targets, then carefully adjusted the imaging conditions to satisfy all three blinking requirements (Table 1) with a high single-molecule localization precision (1.6 nm by DAFL, <1.0 nm from single-molecule fitting, 1.5 nm by theoretical estimate[15], Fig. 4b). See Supplementary Figs 17–21 for details on the imaging quality characterization.

Table 1 | Critical imaging quality parameters for the three blinking requirements.

	Parameter	Value
①	Photon count (×1,000)	50 ± 14
	Localization precision (nm)	1.6 (0.9)
②	Blinking events per target	77 ± 15
	Target signal-to-noise ratio	2.3 ± 1.0
③	Blinking duty cycle per target (%)	0.3
	Fraction of false localizations (%)	8

The localization precision value in brackets was measured by the single-molecule fitting uncertainty.

We used the 20 nm grid structures as drift markers. After applying each step of the drift correction procedure (Fig. 3i), both the 20 nm grid drift markers (Fig. 4c, insets) and 5 nm grid samples (Fig. 4c) became sharper and more regular. We employed two methods for assaying the integral imaging quality: target localization spread (or TLS, carried out by overlaying the localization clouds from well-separated targets and measuring the spread of the overlaid cloud with 2D Gaussian fitting; see Fig. 4d) and Fourier ring correlation (FRC, carried out by computing the correlation between the 2D Fourier transform spectra of independent half images, Fig. 4e). A comparison of the maximal allowable resolution

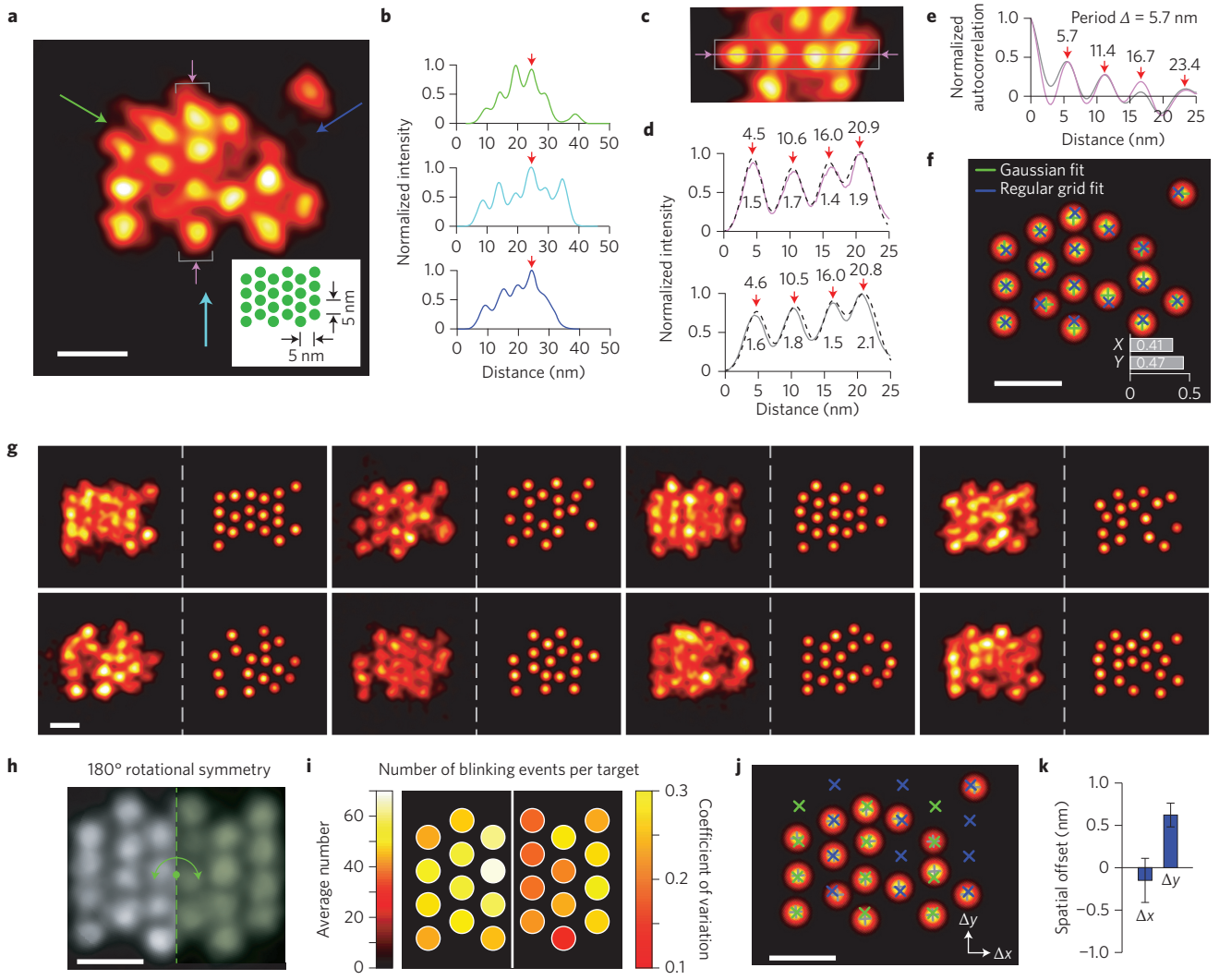

Figure 5 | Discrete molecular imaging of 5 nm grid structure. a, Representative DMI image of a 5 nm triangular grid structure obtained with DNA-PAINT. Inset: Design schematics, where each green dot indicates a docking strand. Arrows indicate the projection directions and areas of study for **b**–**e**. **b**, Intensity projection profiles from the image in **a** along the directions indicated by the colour-matched arrows. The profiles are aligned by the central peaks indicated by red arrows. **c**, Cropped-out image from **a** showing the central region (grey rectangle) and central pixel line (the magenta line and arrows) used for the analysis in **d** and **e**. **d**, Intensity profile along the central line (magenta) and projection from the central region (grey), as indicated by the colour-matched regions in **c**. The four-peak Gaussian fit is shown by the dashed black lines. Numbers indicate the fitted centre positions (top) and the standard deviation values (bottom) for each peak, with an average of 1.7 nm, supporting a 4.0 nm FWHM resolution. **e**, Auto-correlation analysis from the colour-matched profiles in **d**, showing a consistent periodicity of 5.7 nm. **f**, Automatic multitarget fit of the 5 nm grid image in **a**. The crosses indicate Gaussian-fitted centres (green) and regular grid-fitted centres using the green crosses as targets (blue). Inset: r.m.s. deviation between the green and blue crosses (<0.5 nm in 1D and <0.7 nm in 2D). **g**, Representative images of the 5 nm grid structures, showing structural regularity and heterogeneity. For each structure the left panel shows the super-resolution rendered image and the right panel shows the automatic fitted image. **h**, Single-particle class average of the 5 nm grid ($n = 25$). The green dashed line and arrow indicate the axis and operation of symmetry of the structure. **i**, Uniformity of the blinking kinetics as represented on a 5 nm degenerate grid. The colour maps show averages (left) and coefficients of variation (right) of the numbers of blinking events for each distinguishable target. **j**, Automatic multitarget fit (grey) and two-component grid fit of the 5 nm image in **a**, allowing an offset between two groups of targets with opposite staple strand orientations, coloured in green and blue respectively. **k**, Offsets between the two groups of staples in **j** measured from single-molecule images. The error bars indicate standard deviation ($n = 10$). It is important to note that no previous knowledge of the sample structure (the 5 nm grid) was used to produce the above results. The DNA-PAINT imaging conditions used for this experiment were 400 ms frame time, 40,000 total frames and 1 nM imager strand concentration. See Supplementary Figs 17, 22, 23 and Supplementary Methods 5 and 6 for super-resolution images and analysis details, and Supplementary Note 9 for discussions. Scale bars, 10 nm in all panels.

is shown in Fig. 4f—4.3 nm (by TLS) and 3.7 nm (by FRC) after geometry-templated drift correction, which allowed us to estimate the residual drift to be <1 nm (r.m.s.). See Methods for details on image quality characterization.

Plotting the projection profiles along the three symmetry axes of the triangular grid structure further confirmed the DMI imaging quality and the structural regularity of the nanostructures on a representative single-molecule image of a 5 nm grid (Fig. 5a,b). Variations in the peak intensities resulted from missing grid points, which we note again were probably due to nanostructure synthesis defects (see Supplementary Note 9.1 for more details). A projection histogram of the four targets in a central column and the auto-correlation analysis showed an averaged 1.7 nm target standard deviation (equivalent to 4.0 nm resolution in FWHM; Fig. 5c,d) and

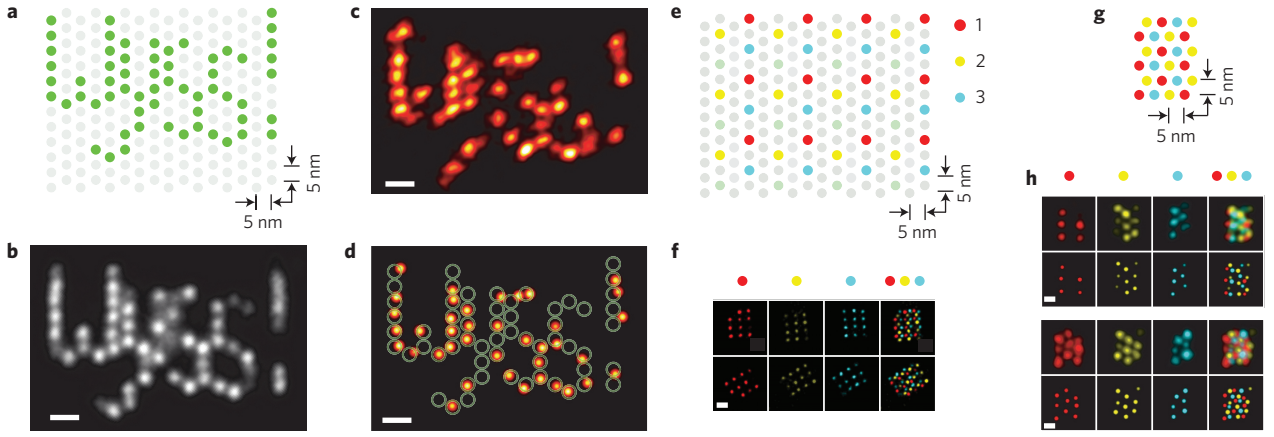

Figure 6 | Discrete molecular imaging with complex patterns and multiplexed visualization. a–d, DMI of a five-character pattern ('Wyss!') on a DNA origami nanodisplay board with 5 nm pixel size. **a**, Design schematics. Each dot indicates a staple strand. Green dots were extended with DNA-PAINT docking strands. **b**, Single-particle class average of the Wyss! pattern ($n = 85$). **c**, A representative single-molecule image of the Wyss! pattern under DMI. **d**, Overlay of the design schematics on top of the automatically fitted single-molecule image in **c**. **e–h**, Three-colour multiplexed DMI, each colour indicates a separate imaging channel with an orthogonal DNA-PAINT sequence. **e**, Design schematic of a three-colour dual-purpose drift and alignment marker. **f**, Cross-channel alignment. Three single-channel images (left three columns) and one composite image (right column) are shown for two example alignment markers. **g**, Design schematics of a three-colour 5 nm grid structure. **h**, Representative multiplexed DMI image of three-colour 5 nm grid pattern in **g**. DNA-PAINT super-resolution images (top row) and automatically fitted images (bottom row) are shown for all three single-colour channels (left three columns) and the combined image (right column) for two representative 5 nm grid structures. The DNA-PAINT imaging conditions used in these experiments are as follows. 'Wyss!' letter pattern image: 500 ms frame time, 100,000 total frames and 0.4 nM imager strand concentration. Multicolour pattern image: 400 ms frame time, 2–3 nM imager strand concentration and 20,000 total frames for each colour channel. See Supplementary Figs 24 and 25 for more super-resolution images, Methods and Supplementary Methods 5 and 6 for the image analysis methods. Scale bars, 10 nm (**b**,**d**,**h**); 20 nm (**f**).

5.7 nm intertarget spacing, consistent with the design (Fig. 5e). We next performed automatic target detection and 2D Gaussian fitting to each target, followed by regular grid fitting to the Gaussian-fitted centres (Fig. 5f, see Methods and Supplementary Methods 6.2 for details). The average deviation between the Gaussian-fitted and grid-fitted centres was measured to be below 1 nm (with a single-target localization precision of 0.18 nm; Fig. 5f).

Each imaging session produced ~50–100 single-molecule images of well-resolved 5 nm grids (Fig. 5g). We next performed single-particle averaging on them and studied the single-molecule imaging heterogeneity among them on the degenerate (half) grid (due to the 180° rotational symmetry; see Fig. 5h, Supplementary Fig. 16 and Supplementary Note 9.2). Specifically, we computed the coefficient of variation in the number of blinking events across different targets in the degenerate grid (0.07) and across different single-molecule images at the same target (0.20). These results demonstrated a relatively uniform imaging efficiency (Fig. 5i, see Supplementary Fig. 22 and Supplementary Methods 6.2 for details), which further supports the hypothesis that the missing grid points probably resulted from strand synthesis or incorporation defects rather than non-uniform imaging efficiency (see Supplementary Note 9.1 for details).

We analysed the origami staple wiring pattern on single-molecule DMI images with ångström-level precision (<2 Å, Fig. 5j,k). By performing an automatic two-component grid fitting algorithm on single-molecule images, we determined the structural offset between two groups of staples with opposing orientations (0.6 ± 0.1 nm), which is consistent with the prediction from structural analysis (0.6 nm, see Supplementary Fig. 23 for details).

DMI in complex and multiplexed samples

We also demonstrated DMI in a complex arrangement by constructing and visualizing a custom-designed letter pattern ('Wyss!') on the 60×85 nm origami nanodisplay breadboard with 5 nm display pixel size (Fig. 6a and Supplementary Fig. 24). The single-particle class average showed an average resolution of 4.6 nm in FWHM, allowing the visualization of individual targets (Fig. 6b). A representative single-molecule super-resolution image (Fig. 6c) displays individually distinguishable targets arranged in the designed pattern (Fig. 6d).

Multiplexed DMI further requires accurate registration between multiple imaging channels. For example, to achieve 5 nm imaging resolution, <1 nm registration accuracy is required. Traditional multitarget imaging and colocalization studies on molecular scale rely on registration between multiple spectral channels and either require a specialized and complicated hardware set-up and calibration process, and hence could be practically difficult to extend beyond two-colour registration or to the entire field of view, or achieve a suboptimal registration accuracy that does not allow molecular resolution imaging[21,40].

We combined DMI with Exchange-PAINT[10] and demonstrated highly accurate (<1 nm) three-colour registration, in addition to highly accurate drift correction (<1 nm r.m.s.) within each channel. The method uses only one fluorophore and one optical path, thus greatly simplifies cross-channel registration and naturally extends to the entire field of view. To implement this method, we first designed a three-colour nanogrid dual-purpose drift and alignment marker, where each colour comprises a regular square grid with 20 nm lattice spacing, similar to the 20 nm grid used above (Fig. 6e). We designed three orthogonal imager sequences with optimized binding on-time, and labelled the substructure in each colour with a unique sequence. We performed multiplexed DMI imaging through serial buffer exchange (Exchange-PAINT), and then performed drift correction using these dual-purpose markers for each channel individually, followed by cross-channel alignment between each pair of different colours (Fig. 6f, see Methods, Supplementary Fig. 25 and Supplementary Methods 6.2 for details). The high-precision visualization of individual targets (down to the ångström level, as shown above) allows highly accurate alignment across all channels (<1 nm), enabling DMI imaging (Fig. 6f).

We then imaged a three-colour mixture structure of the 5 nm grid with multiplexed DMI with an average DAFL localization precision of 2.0 nm and a TLS resolution of 5.9 nm in FWHM (Fig. 6g,h, Supplementary Fig. 25). Automatic target fitting to single-molecule structures revealed the regular grid pattern as designed.

Conclusion

DMI differs from current super-resolution fluorescence microscopy techniques in a similar manner to digital versus analogue signal processing. Whereas current super-resolution demonstrations typically focus on depicting the continuous morphology of macromolecular structures and the biomolecule spatial distributions (analogue)[22,26,41–43] with the resolution limited by the sampling density (the Nyquist sampling criterion), DMI imaging aims at discrete visualization of each individual molecular component within these structures. Combined with the high multiplexing power of Exchange-PAINT, DMI could potentially enable the determination of the position and identity of each molecular component in a complex biological or synthetic nanoscale system, and thus offers a complementary method to electron microscopy and crystallography with single-molecule sensitivity. Furthermore, the ångström-level precision (<2 Å) structural study of DNA nanostructures suggests that DMI could be applicable to studying submolecular and even potentially atomic-level features (for example, the macromolecular composition and component positions, geometric distortions and conformational changes).

We see two challenges in the further development of DMI. The first comes from the physical trade-off between spatial and temporal resolution[13,26]. Specifically, achieving higher spatial resolutions requires longer blinking on-times, a larger number of blinking events and a lower blinking on–off duty cycle—all of which necessarily increase the total image acquisition time. Potential ways to shorten the imaging time include engineering brighter fluorophores to shorten the blinking on-time required to collect enough photons. The second challenge is imposed by the imperfect labelling of biomolecular targets. Although our method is not limited by the Nyquist sampling criterion (the number of probes labelled per unit space), it is still limited by the absolute labelling efficiency (the average number of probes labelled per molecular target). Conventional immunostaining methods with IgG antibodies both introduce a large offset from the target epitope to the chemically conjugated probe (~10 nm) and often have limited labelling efficiencies (due to the large size and sometimes the low affinity of the antibodies). Several approaches could potentially address these issues: genetically labelled tags (for example SNAP-tags, unnatural amino acids) can provide a smaller probe size and higher labelling efficiency; aptamers, small-molecule labels, single-chain antibody fragments and camelid single-chain antibodies (nanobodies) could also provide effective alternatives for smaller affinity probes.

DMI allows the direct visualization of each individual component in densely packed biomolecular environment. In the future, we expect the development of DMI to eventually allow quantitative molecular features to be studied in diverse biological systems such as the molecular composition and architecture of diverse cellular systems (for example, cell membrane receptor clusters, neuronal synapses), the molecular states of individual protein components within macromolecular context (for example, the binding and rotational states of ring ATPase complexes, patterns of histone modifications) and the 3D architecture of chromosomes with high spatial and genomic resolution.

Methods

Methods and any associated references are available in the online version of the paper.

Received 2 December 2015; accepted 9 May 2016; published 4 July 2016

References

1. Hell, S. W. & Wichmann, J. Breaking the diffraction resolution limit by stimulated emission: stimulated-emission-depletion fluorescence microscopy. *Opt. Lett.* **19,** 780–782 (1994).
2. Klar, T. A. & Hell, S. W. Subdiffraction resolution in far-field fluorescence microscopy. *Opt. Lett.* **24,** 954–956 (1999).
3. Gustafsson, M. G. Surpassing the lateral resolution limit by a factor of two using structured illumination microscopy. *J. Microsc.* **198,** 82–87 (2000).
4. Gustafsson, M. G. Nonlinear structured-illumination microscopy: wide-field fluorescence imaging with theoretically unlimited resolution. *Proc. Natl Acad. Sci. USA* **102,** 13081–13086 (2005).
5. Betzig, E. *et al.* Imaging intracellular fluorescent proteins at nanometer resolution. *Science* **313,** 1642–1645 (2006).
6. Hess, S. T., Girirajan, T. P. & Mason, M. D. Ultra-high resolution imaging by fluorescence photoactivation localization microscopy. *Biophys. J.* **91,** 4258–4272 (2006).
7. Rust, M. J., Bates, M. & Zhuang, X. Sub-diffraction-limit imaging by stochastic optical reconstruction microscopy (STORM). *Nature Methods* **3,** 793–795 (2006).
8. Heilemann, M. *et al.* Subdiffraction-resolution fluorescence imaging with conventional fluorescent probes. *Angew. Chem. Int. Ed.* **47,** 6172–6176 (2008).
9. Sharonov, A. & Hochstrasser, R. M. Wide-field subdiffraction imaging by accumulated binding of diffusing probes. *Proc. Natl Acad. Sci. USA* **103,** 18911–18916 (2006).
10. Jungmann, R. *et al.* Multiplexed 3D cellular super-resolution imaging with DNA-PAINT and Exchange-PAINT. *Nat. Methods* **11,** 313–318 (2014).
11. Hell, S. W. Microscopy and its focal switch. *Nat. Methods* **6,** 24–32 (2009).
12. Huang, B., Bates, M. & Zhuang, X. Super-resolution fluorescence microscopy. *Ann. Rev. Biochem.* **78,** 993–1016 (2009).
13. Sahl, S. J. & Moerner, W. E. Super-resolution fluorescence imaging with single molecules. *Curr. Opin. Struct. Biol.* **23,** 778–787 (2013).
14. Moerner, W. E. & Kador, L. Optical detection and spectroscopy of single molecules in a solid. *Phys. Rev. Lett.* **62,** 2535–2538 (1989).
15. Russell, E. T., Daniel, R. L. & Watt, W. W. Precise nanometer localization analysis for individual fluorescent probes. *Biophys. J.* **82,** 2775–2783 (2002).
16. Löschberger, A. *et al.* Super-resolution imaging visualizes the eightfold symmetry of gp210 proteins around the nuclear pore complex and resolves the central channel with nanometer resolution. *J. Cell Sci.* **125,** 570–575 (2012).
17. Szymborska, A. *et al.* Nuclear pore scaffold structure analyzed by super-resolution microscopy and particle averaging. *Science* **341,** 655–658 (2013).
18. Yildiz, A. *et al.* Myosin V walks hand-over-hand: single fluorophore imaging with 1.5-nm localization. *Science* **300,** 2061–2065 (2003).
19. Rittweger, E., Han, K., Irvine, S. E., Eggeling, C. & Hell, S. W. STED microscopy reveals crystal colour centres with nanometric resolution. *Nature Photon.* **3,** 144–147 (2009).
20. Shtengel, G. *et al.* Interferometric fluorescent super-resolution microscopy resolves 3D cellular ultrastructure. *Proc. Natl Acad. Sci. USA* **106,** 3125–3130 (2009).
21. Pertsinidis, A., Zhang, Y. & Chu, S. Subnanometre single-molecule localization, registration and distance measurements. *Nature* **466,** 647–651 (2010).
22. Vaughan, J. C., Jia, S. & Zhuang, X. Ultrabright photoactivatable fluorophores created by reductive caging. *Nat. Methods* **9,** 1181–1184 (2012).
23. Raab, M., Schmied, J. J., Jusuk, I., Forthmann, C. & Tinnefeld, P. Fluorescence microscopy with 6 nm resolution on DNA origami. *Chemphyschem* **15,** 2431–2435 (2014).
24. Kaplan, C. *et al.* Absolute arrangement of subunits in cytoskeletal septin filaments in cells measured by fluorescence microscopy. *Nano Lett.* **15,** 3859–3864 (2015).
25. Fernández-Suárez, M., Chen, T. S. & Ting, A. Y. Protein-protein interaction detection in vitro and in cells by proximity biotinylation. *J. Am. Chem. Soc.* **130,** 9251–9253 (2008).
26. Shroff, H., Galbraith, C. G., Galbraith, J. A. & Betzig, E. Live-cell photoactivated localization microscopy of nanoscale adhesion dynamics. *Nat. Methods* **5,** 417–423 (2008).
27. Dempsey, G. T., Vaughan, J. C., Chen, K. H., Bates, M. & Zhuang, X. Evaluation of fluorophores for optimal performance in localization-based super-resolution imaging. *Nat. Methods* **8,** 1027–1036 (2011).
28. Xu, K., Babcock, H. P. & Zhuang, X. Dual-objective STORM reveals three-dimensional filament organization in the actin cytoskeleton. *Nat. Methods* **9,** 185–188 (2012).
29. Giannone, G. *et al.* Dynamic superresolution imaging of endogenous proteins on living cells at ultra-high density. *Biophys. J.* **99,** 1303–1310 (2010).
30. Schoen, I., Ries, J., Klotzsch, E., Ewers, H. & Vogel, V. Binding-activated localization microscopy of DNA structures. *Nano Lett.* **11,** 4008–4011 (2011).

31. Jungmann, R. *et al.* Single-molecule kinetics and super-resolution microscopy by fluorescence imaging of transient binding on DNA origami. *Nano Lett.* **10,** 4756–4761 (2010).
32. Johnson-Buck, A. *et al.* Super-resolution fingerprinting detects chemical reactions and idiosyncrasies of single DNA pegboards. *Nano Lett.* **13,** 728–733 (2013).
33. Iinuma, R. *et al.* Polyhedra self-assembled from DNA tripods and characterized with 3D DNA-PAINT. *Science* **344,** 65–69 (2014).
34. Nieuwenhuizen, R. P. *et al.* Measuring image resolution in optical nanoscopy. *Nature Methods* **10,** 557–562 (2013).
35. Cordes, T. *et al.* Resolving single-molecule assembled patterns with superresolution blink-microscopy. *Nano Lett.* **10,** 645–651 (2010).
36. Thompson, M. A., Lew, M. D. & Moerner, W. E. Extending microscopic resolution with single-molecule imaging and active control. *Annu. Rev. Biophys.* **41,** 321–342 (2012).
37. Rothemund, P. W. Folding DNA to create nanoscale shapes and patterns. *Nature* **440,** 297–302 (2006).
38. Schmied, J. *et al.* Fluorescence and super-resolution standards based on DNA origami. *Nature Methods* **9,** 1133–1134 (2012).
39. Alushin, G. M. *et al.* High-resolution microtubule structures reveal the structural transitions in αβ-Tubulin upon GTP hydrolysis. *Cell* **157,** 1117–1129 (2014).
40. Pertsinidis, A. *et al.* Ultrahigh-resolution imaging reveals formation of neuronal SNARE/Munc18 complexes *in situ*. *Proc. Natl Acad. Sci. USA* **110,** E2812–E2820 (2013).
41. Chmyrov, A. *et al.* Nanoscopy with more than 100,000 'doughnuts'. *Nat. Methods* **10,** 737–740 (2013).
42. Xu, K., Zhong, G. & Zhuang, X. Actin, spectrin, and associated proteins form a periodic cytoskeletal structure in axons. *Science* **339,** 452–456 (2013).
43. Dong, L. *et al.* Extended-resolution structured illumination imaging of endocytic and cytoskeletal dynamics. *Science* **349,** aab3500 (2015).

Acknowledgements

We thank M. Avendaño, J. Wöhrstein, F. Schüder, G. Church, W. Shih, D. Zhang, S. Agasti, E. Winfree and P. Rothemund for helpful discussions, and C. Myhrvold, N. Liu, W. Sun, X. Chen, F. Vigneault and H. Tang for helpful comments on the manuscript. This work is supported by a National Institutes of Health (NIH) Director's New Innovator Award (1DP2OD007292), an NIH Transformative Research Award (1R01EB018659), an NIH grant (5R21HD072481), an Office of Naval Research (ONR) Young Investigator Program Award (N000141110914), ONR grants (N000141010827 and N000141310593), a National Science Foundation (NSF) Faculty Early Career Development Award (CCF1054898), an NSF grant (CCF1162459) and a Wyss Institute for Biologically Engineering Faculty Startup Fund to P.Y. M.D. acknowledges support from the HHMI International Predoctoral Fellowship. R.J. acknowledges support from the Alexander von Humboldt-Foundation through a Feodor-Lynen Fellowship.

Author contributions

M.D. conceived of and designed the study, designed and performed the experiments, developed the software, analysed the data and wrote the manuscript. R.J. conceived of and designed the study, interpreted the data and critiqued the manuscript. P.Y. conceived of, designed and supervised the study, interpreted the data and wrote the manuscript. All authors reviewed and approved the manuscript.

Additional information

Supplementary information is available in the online version of the paper. Reprints and permissions information is available online at www.nature.com/reprints. Correspondence and requests for materials should be addressed to P.Y.

Competing financial interests

The authors have filed a patent application. P.Y. and R.J. are co-founders of Ultivue, Inc., a start-up company with interests in commercializing the reported technology.

Methods

Materials and buffers. Unmodified and biotin-labelled DNA oligonucleotides were purchased from Integrated DNA Technologies. Fluorescently modified DNA oligonucleotides were purchased from Biosynthesis. Streptavidin was purchased from Invitrogen (catalog number S-888). Biotinylated bovine serum albumin (BSA-biotin, catalog number A8549), Protocatechuate 3,4-Dioxygenase (PCD, catalog number P8279), Protocatechuic acid (PCA, catalog number 37580) and 6-Hydroxy-2,5,7,8-tetramethylchromane-2-carboxylic acid (Trolox, catalog number 238813) were purchased from Sigma-Aldrich. Glass slides and coverslips were purchased from VWR. The M13mp18 scaffold was purchased from New England BioLabs. Freeze 'N Squeeze columns were purchased from Bio-Rad.

The following buffers were used for sample preparation and imaging: DNA origami folding buffer (12.5 mM $MgCl_2$, 1× TE buffer), buffer A (10 mM Tris-HCl, 100 mM NaCl, 0.1% (v/v) Tween 20, pH 8.0), buffer B (10 mM Tris-HCl, 10 mM $MgCl_2$, 1 mM EDTA, 0.1% (v/v) Tween 20, pH 8.0) and buffer TP (1× buffer B, 10 nM PCD, 2.5 mM PCA, 1 mM Trolox).

Fluorescence microscopy set-up. Fluorescence imaging was carried out on an inverted Nikon Eclipse Ti microscope (Nikon Instruments) with the Perfect Focus System, applying an objective-type TIRF configuration using a Nikon TIRF illuminator with an oil-immersion objective (CFI Apo TIRF 100×, numerical aperture (NA) 1.49). Laser excitation with a 561 nm laser (200 mW, Coherent Sapphire) was passed through a clean-up filter (ZET561/10, Chroma Technology) and coupled into the microscope using a beam splitter (ZT488rdc/ZT561rdc/ZT640rdc, Chroma Technology). Fluorescence light was spectrally filtered with emission filter (ET60050m, Chroma Technology). Super-resolution movies were recorded with either an electron multiplying charge-coupled device (EMCCD, used without EM gain option) camera (iXon X3 DU-897, Andor Technologies) or a scientific complementary metal-oxide–semiconductor device (sCMOS) camera (Zyla 4.2, Andor Technologies).

Simulation of the microscopy data set. Simulation of the microscopy data sets was performed with custom-written MATLAB software for Figs 1, 3 and Supplementary Fig. 3, with realistic parameters determined from fluorescence microscopy experiments, including image and pixel sizes, camera conversion factor and noise level, fluorophore photon emission rate and imaging background noise. Stochastic and independent blinking kinetics was simulated for all images apart from the first two blinking requirement tests in Supplementary Fig. 3. Intensity distributions from single-molecule blinking events were generated with finite pixel approximation of Gaussian profiles and corrupted with Poisson noise and Gaussian background and readout noise. See Supplementary Methods 2 for more details.

Imaging quality characterization for three blinking requirements. For blinking requirement (1) the photon count was calculated by converting camera counts to photons using camera manufacture-provided conversion factor. The localization precision was characterized by two methods. DAFL was calculated for pairs of localizations that originated from the same blinking events but were separated into two adjacent frames; the distribution of all of the distances between the pairs was fitted to the theoretical distribution function and the localization precision was determined from the fit. The Gaussian fitting uncertainty reports the Cramer–Rao lower bound (CRLB) for 2D Gaussian fitting for each localization[44].

For blinking requirement (2) the number of blinking events was calculated for each imaging target from the single-molecule blinking time trace by counting the number of on–off switchings within the time trace. The target SNR was calculated for each pair of neighbouring targets by either automatically or manually selecting a region of interest that enclosed both targets and computing the localization distribution along the axis connecting them; two-peak Gaussian fitting was performed and the peak-to-valley distance and residual noise were used as signal and noise.

For blinking requirement (3) the blinking duty cycle was calculated for each structure from the structure's blinking time trace by calculating the characteristic on-time and off-time respectively. These were obtained by fitting the cumulative distribution of all on- and off-times both of and between blinking events to the expected distribution functions. False localizations were determined from abnormally high photon counts by a photon count threshold (2σ above the mean photon count). The effective localizations for the simulations were determined by a distance cutoff between the localized position and the simulated (true) positions with a 3σ threshold.

For each 10 nm comparison structure under each imaging condition the corresponding technical requirement was measured using the methods described above. In addition, a projection histogram from the marked region in the image was generated and fitted to a multi-peak Gaussian distribution. See Supplementary Fig. 3 and Supplementary Methods 3 for more details regarding these methods.

DNA origami design and self-assembly. All DNA origami nanostructures were designed with the caDNAno software[45], and were based on a twist-corrected variant of the rectangular structure[37] (see Supplementary Tables 1–5 for the sequence details). The DNA origami structures used as imaging standards with specific dimensions (20 nm square grid, 10 nm comparison standards and 5 nm triangular grid) were designed on the basis of length measurements from AFM (Supplementary Fig. 4). Eight staple strands were biotin-modified for surface fixation. Drift marker structures used in the 20 nm comparison pattern experiments were folded with DNA-PAINT extension on all possible staple strands. Staple strands used as imaging targets were extended with DNA-PAINT docking sequences (7–10 nt in length) with one or two thymine base(s) spacers. See Supplementary Figs 4–6 for more details.

The DNA origami 20 nm square grid structures were self-assembled in a one-pot annealing reaction with 50 µl total volume containing 10 nM scaffold strand (m13mp18), 100 nM unmodified staple strands, 120 nM biotin-modified strands and 1 µM strands with DNA-PAINT extensions in DNA origami folding buffer. Drift markers for 20 nm grid image were self-assembled with 400 nM of all of the staple strands with DNA-PAINT extensions. The 10 nm comparison patterns, 5 nm grid and 'Wyss!' pattern structures were self-assembled with 500 nM biotin-modified staple strands and 1 µM staple strands with DNA-PAINT extensions. The three-colour 5 nm grid structure was self-assembled with 120 nM biotin-modified staple strands and 1 µM staple strands with DNA-PAINT extensions. For the 20 nm square grid and 10 nm comparison pattern structures the solution was annealed with a thermal ramp cooling from 90 °C to 25 °C over the course of 75 min. For the 5 nm grid and 'Wyss!' pattern structures, the solution was annealed with a thermal ramp cooling from 90 °C to 20 °C over the course of 3 h and for the three-colour 20 nm grid and 5 nm grid structures the solution was annealed with a thermal ramp cooling from 90 °C to 20 °C over the course of 72 h.

The self-assembled DNA origami structures were characterized and purified (except for the 20 nm square grid structures) by agarose gel electrophoresis (2% agarose, 0.5× TBE, 10 mM $MgCl_2$, 0.5× SybrSafe pre-stain) at 4.5 V cm^{-1} for 1.5 h. For purification, the gel bands were cut, crushed and filled into a Freeze 'N Squeeze column and spun for 10 min at 800*g* at 4 °C.

DNA-PAINT sample preparation and imaging. DNA-PAINT sample preparation was performed in custom-constructed flow chambers between a piece of coverslip and a glass slide or on a commercial flow chamber slide (ibidi). Sample structures were fixed on the surface via a biotin–streptavidin–biotin bridge by serially flowing BSA-biotin (1.0 mg ml^{-1}), streptavidin (0.5 mg ml^{-1}) and biotin-labelled samples. The sample concentration was calibrated for different structure and imager combinations to make sure that similar numbers of blinking events are detected per camera frame. The flow chamber was filled with an imaging buffer (an appropriate concentration of dye-labelled imager strands in buffer TP) and incubated for 10 min before imaging. For imaging with the custom-constructed flow chambers the flow chamber was sealed with epoxy glue before imaging. See Supplementary Methods 4 for the flow chamber protocol details and Supplementary Table 6 for the imager sequences.

Exchange-PAINT imaging for the three-colour samples was performed based on protocol adapted from our previous work[10]. In brief, the DNA origami sample was prepared in a flow chamber and a buffer exchange was performed by serially flowing in 400 µl of buffer B and then 200 µl of the next imaging buffer into the imaging chamber.

DNA-PAINT super-resolution imaging. DNA-PAINT super-resolution movies for the 10 nm standard patterns were captured with 5 Hz camera frame rate (200 ms per frame) for all images. The laser intensity was varied from 0.3–1.0 kW cm^{-2} before and after meeting requirement (1). The imaging length was varied from 2,500 to 12,500 frames before and after meeting requirement (2), and to 40,000 frames after meeting requirement (3). The imager concentration was varied from 20 nM to 5 nM before and after meeting requirement (3). DNA-PAINT movies for the 'best condition' 10 nm standard patterns in Fig. 2 was captured with 4 Hz camera frame rate (250 ms per frame) for (b) and (c), 2.5 Hz frame rate (400 ms) for (d); 30,000 total imaging frames for (b) and (c), 50,000 frames for (d); 15 nM imager concentration for (b) and (c) and 5 nM for (d). The laser intensity was 1.0 kW cm^{-2} for all images. DNA-PAINT movies for the 20 nm grid images were captured with 3.3 Hz camera frame rate (300 ms per frame), with 1.0 kW cm^{-2} laser intensity, and 3 nM of dye-labelled imager strand for 30,000 frames. DNA-PAINT movies for the 5 nm grid images were captured with 2.5 Hz camera frame rate (400 ms per frame), with 1.0 kW cm^{-2} laser intensity and 1 nM of dye-labelled imager strand for 40,000 frames. The DNA-PAINT movie for the 'Wyss!' pattern was captured with 2 Hz frame rate (500 ms) and 0.4 nM imager strand concentration for 100,000 frames. The DNA-PAINT movie for the three-colour 5 nm grid was captured with 2.5 Hz frame rate (400 ms) and 2–3 nM imager strand concentrations with 20,000 frames per colour.

Extra drift markers were supplemented for some images. For the 20 nm grid structure, extra drift markers with DNA-PAINT docking extensions on all strands were used. For the 10 nm two-target structure, 5 nm grid and 'Wyss!' pattern images, extra drift markers of the 20 nm grid structures were used. For the three-colour 5 nm grid images, further dual-purpose drift and alignment markers of the three-colour 20 nm grid structures were used.

Super-resolution data processing and image analysis. DNA-PAINT super-resolution movies were processed with custom-written MATLAB software. In general, images were processed and analysed in three steps: (i) spot detection and

localization, (ii) drift correction, (iii) super-resolution rendering and quality analysis. Spot detection and localization was performed with efficient and accurate Gaussian fitting algorithms as reported in ref. 44. For the 10 nm comparison pattern images, drift correction was performed with simple trace averaging only. For the 20 nm grid, 5 nm grid, Wyss! pattern and three-colour 5 nm grid images, drift correction was performed with simple trace averaging followed by templated and geometry-templated drift correction methods with the 20 nm grid markers, as described in the sections below. For the three-colour 5 nm grid images, alignment across different channels was performed following drift correction procedures with the same three-colour 20 nm grid dual-purpose markers described in sections below. The imaging quality was characterized separately for each of the three DMI requirements and for the final super-rendered image by a variety of methods, as described below. Final super-resolution images were rendered with Gaussian blurring with the standard deviation set to the estimated localization precision. A simplified version of the software processing suite can be obtained at http://molecular.systems/software or http://www.dmi-imaging.net. See Supplementary Methods 5 and 6 for more details.

DNA nanostructure-based drift correction. Drift compensation based on the DNA origami marker structures was performed using the following steps. First we selected (either automatically or manually) a pool of isolated structures as drift markers (either the 20 nm grid markers, all-modified drift markers or the samples themselves) and took a simple trace average of their blinking time traces as the drift correction trace. This was the only drift correction method used for the 10 nm comparison patterns images. For the 20 nm grid, 5 nm grid, Wyss! pattern and the three-colour 5 nm grid samples, templated drift correction and geometry-templated drift correction methods were then performed with the aid of 20 nm origami grid markers in a frame-by-frame manner. For each frame, the algorithm identified all of the localizations and assigned an 'offset vector' to each, to be used for averaging. A photon-weighted global average of all of the calculated offset vectors was used for drift correction of the current frame. In the templated drift correction method the offset vector was determined from the localization position in relation to the target site position, which was determined by a local 2D Gaussian fitting of all of the localizations originated from that target. In geometry-templated drift correction method the offset vector was determined from the localization position relative to the regular 20 nm grid-fitted target position instead of the Gaussian-fitted target position. The remaining drift in the corrected images was estimated by comparing the maximal allowed imaging resolution (measured by the DAFL localization precision) and the measured imaging resolution (either by Gaussian fitting of the single-particle averaged image or by the TLS method, see below) using the quadratic sum principle. It is important to note that in producing the 5 nm grid, the 'Wyss!' pattern and the three-colour 5 nm grid images, no previous information about the sample structures was used for the templated and geometry-templated drift correction procedures. See Supplementary Methods 5.2 for more details.

Imaging quality characterization for super-rendered images. The imaging resolution for super-rendered images was characterized using a few methods. Target localization spread (TLS) was calculated by overlaying the localization cloud for all of the separable targets on top of each other, aligned by the centre of mass position, and measuring the standard deviation of the overlaid cloud of localizations; the FWHM value was reported as the resolution estimate. Fourier ring correlation (FRC) was calculated by splitting the image into two independent half images by cutting the super-resolution movie stack into sections of ~100 frames and arbitrarily assigning half of the sections to each half image. The spatial frequency correlation between their respective 2D fast Fourier transform (FFT) spectra was calculated and the crossover point with the noise-based 2σ threshold curve was reported as the supported imaging resolution. See Supplementary Methods 6.1 for more details.

Single-particle class averaging analysis. The single-particle averaging analysis was carried out with the EMAN2 software package (version 2.0). Images of the individual particles were automatically selected and super-rendered with a pixel size set to less than the localization precision in a custom MATLAB program and processed with a reference free class averaging functionality in EMAN2 (e2refine2d), allowing only rotational and translational transformations during alignment. A number of particles were used for the averaging ($N = 700$ for the 20 nm square lattice, $N = 25$ for the 5 nm grid standard and $N = 85$ for the Wyss! pattern) and from each session the most representative class average image was selected as the final result. See Supplementary Methods 6.2 for more details.

Automatic fitting, regular grid fitting and cross-channel alignment. Automatic fitting was performed on the 20 nm grid (single-particle class average), the 5 nm grid (non-averaged single-molecule), the 'Wyss!' pattern (non-averaged single-molecule) and the three-colour 5 nm grid (non-averaged single-molecule) images. Spot detection was performed after a Gaussian filter was used to suppress the background variation. Automatic 2D Gaussian fitting was performed for each detected centre with a fixed standard deviation determined by the overall image resolution. The fitted image was rendered with the fitted positions and intensity values.

Regular grid fitting analysis was carried out for the 20 nm grid (single-particle class average) and the 5 nm grid (both non-averaged super-resolution images and single-particle class average) with an automatic algorithm based on the individually fitted centres (above). The grid geometry (a square lattice for 20 nm grid and a triangular lattice for 5 nm grid) and number of grid points were input manually and an initial estimate of the grid boundaries was also manually set to reduce the fitting time. The best fitted grid was determined by minimizing the r.m.s. deviation of the fitted points.

Cross-channel alignment with three-colour 20 nm grid alignment markers was performed by applying automatic fitting and regular grid fitting to all three substructures of the alignment marker and recording the offset between their fitted positions. The cross-channel registration offset was then calculated by comparing the recorded offset with the pre-designed offset across different channels. A number of (>10) high-quality alignment markers were identified and their offset computed in this way; the average from all of them was used as the final registration offset. See Supplementary Methods 6.2 for more details.

References

44. Smith, C. S., Joseph, N., Rieger, B. & Lidke, K. A. Fast, single-molecule localization that achieves theoretically minimum uncertainty. *Nature Methods* **7,** 373–375 (2010).
45. Douglas, S. M. *et al.* Rapid prototyping of 3D DNA-origami shapes with caDNAno. *Nucl. Acids Res.* **37,** 5001–5006 (2009).